communications biology

Article

https://doi.org/10.1038/s42003-024-07317-9

Quantitative single-molecule analysis of assembly and Ca^{2+}-dependent disassembly of synaptotagmin oligomers on lipid bilayers

Check for updates

Feng Li[1,2], Jeff Coleman[1,2], Lorena Redondo-Morata[3], R. Venkat Kalyana Sundaram[1,2], Ekaterina Stroeva[1,2], James E. Rothman[1,2] ✉ & Frédéric Pincet[1,2,4] ✉

Synaptotagmin-1 (Syt-1) self-assembles into ring-like oligomers, and genetic and biochemical evidence suggest that oligomerization is needed to clamp synaptic vesicles and stabilize them for Ca^{2+}-evoked release. However, oligomerization has not yet been demonstrated on lipid bilayers or studied in quantitative biophysical terms. Here we utilize single-molecule imaging methods to monitor the assembly and disassembly of oligomeric clusters of Syt-1 on lipid bilayers in real-time. Syt-1 assembled into two distinct classes of oligomers, small (5 ± 2 subunits) and large (15 ± 2 subunits). Each class assembled at a constant k_{on} that was always proportional to its ultimate size, but both classes disassembled at the same unit rate (k_{off}) independent of its size. Both large and small oligomers explosively disassembled when Ca^{2+} was added. The F349A mutation in the Syt-1 nearly eliminates the large class of oligomers but does not reduce the small class. Altogether, the physical-chemical properties of Syt-1 oligomers meet or exceed the physiologic requirements to function as such a clamp.

The synaptic proteins Munc13-1 and Synaptotagmin-1 (Syt-1) form oligomers with well-defined structures and shapes[1–9]. Munc13-1 is the key molecular chaperone that assembles the SNARE complex[10–14] and transitions between distinct oligomeric states to scaffold the assembly of the ready-release synaptic vesicle in several steps[9,15,16]. Syt-1 is the primary calcium sensor triggering synchronous release of these primed synaptic vesicles[17–24].

Oligomers of Syt-1 have a ring-like shape, suggesting a potential role as a clamp to reduce the spontaneous fusion of docked vesicles[25–30]. In particular, Wang et al. reported the assembly of Sytnaptotagmin-1 into ring-like structures on lipid monolayers using negative staining electron microscopy[3]. The rings were also observed to self-assemble in solution in the presence of Mg^{2+} and phosphatidylinositol 4,5-bisphosphate diC_4 or Mg^{2+} and ATP[28]. Fluorescence correlation microscopy studies revealed that the average copy number of Syt-1 in these oligomers to be ~16 molecules[28].

A targeted mutation (F349A) selectively disrupts the interfacial interaction between neighboring Synaptotagmin-1 molecules, thereby preventing rings from assembling[29,30]. This mutation greatly increases spontaneous release of synaptic vesicles from PC12 neuro-endocrine cells[29] and increases all forms of release at cortical synapses[30], confirming the idea that Syt-1 rings function to restrain (i.e., clamp) synaptic vesicles from fusing. Cryo-electron tomography of the synaptic vesicle–plasma membrane interface in PC12 cells revealed a circular, symmetrical arrangement of 6 protein complexes that was also disrupted by expressing the ring-disrupting F349 Syt-1 mutant protein that caused spontaneous release[31]. A follow-up study[32] measuring average changes in populations of boutons failed to detect meaningful effects of F349A, most likely the result of population averaging, but did confirm that Synaptotagmin oligomerization is a primary mechanism for clamping and provided novel evidence that the juxta-membrane linker region may also contribute to oligomerization. In vitro functional studies using reconstituted single vesicle analysis found that vesicles containing F349A diffuse freely on the bilayer and undergo spontaneous fusion[25], while vesicles with wild type Syt-1 are immobile on the bilayer until fusion is triggered by Ca^{2+}, strongly suggesting that Syt-1 oligomers clamp the fusion machinery.

[1]Department of Cell Biology, School of Medicine, Yale University, 333 Cedar Street, New Haven, CT, 06520, USA. [2]Nanobiology Institute, Yale West Campus Yale University, West Haven, CT, 06516, USA. [3]Aix-Marseille University, INSERM, DyNaMo, Turing centre for living systems, Marseille, France. [4]Laboratoire de Physique de l'Ecole normale supérieure, ENS, Université PSL, CNRS, Sorbonne Université, Université de Paris, F-75005 Paris, France.
✉e-mail: james.rothman@yale.edu; frederic.pincet@ens.fr

While these studies have been important in suggesting a key role for circular oligomers of Syt-1 in regulating neurotransmitter release, the observations to date are largely qualitative and concern oligomers forming on artificial lipid monolayers or in solution, neither being directly physiologically relevant; and oligomers have not yet been directly demonstrated to form on more physiologically relevant lipid bilayers. A quantitative understanding is also required, including determining their size distributions in greater detail and, critically, acquiring energetic and kinetic information about the assembly and disassembly processes. Furthermore, the behavior of Syt-1 oligomers in response to Ca^{2+} remains poorly understood. Such knowledge is crucial in assessing whether the formation of a Syt-1 ring-based clamp can occur within the required time frame; whether this clamp can persist long enough to establish a readily-releasable pool, and whether it can dissipate fast enough to allow synchronous Ca^{2+}-evoked fusion. Each of these factors is essential for an effective clamp in neurotransmission.

Hence the general physiological relevance of Syt oligomerization to control of neurotransmitter release has already been established[29,30]. Here, we provide a detailed physical chemical description of the oligomerization process and its control by calcium ions. We employ single molecule methods on a well-defined bilayer system to establish the size distribution of oligomeric Syt-1 clusters as well as the real-time kinetics of oligomerization and dissociation. We have identified kinetically distinct small (5 ± 2) and large (15 ± 2) clusters which assemble on bilayers at equilibrium. Their sizes are determined by their differing rates of association, rather than their rates of dissociation, which are the same. The F349A "unclamping" mutation eliminates the large but not the small clusters, suggesting that the large clusters are more relevant to regulating neurotransmitter release. Both types of clusters rapidly disassemble when exposed to Ca^{2+} ions.

Results

Syt-1 molecules form clusters on lipid bilayers

Syt-1 has an N-terminal transmembrane domain and its cytosolic part includes a linker domain (residues 79 to 142) followed by two C2 domains (C2A and C2B, residues 143 to 421) at the C-terminus. We bacterially-expressed and then purified the complete cytosolic domain, including the linker domain[32], consisting of residues 79-421, with the native Cys at residue 79 for fluorescent labelling[33] and His_6-SUMO at the N-terminus to facilitate purification (Supplementary Figs. S1 & S2; also see Materials and Methods for details).

The AlexaFluor 647-labelled cytosolic Syt-1 (55 *nM*) was incubated at 23 °C with a supported lipid bilayer containing 71 mole% DOPC, 25% DOPS, 2% $PI(4,5)P_2$, and 2% DAG in a buffer solution containing 50 mM HEPES, 140 mM KCl, 10% glycerol, and 1 mM TCEP and then examined by TIRF microscopy (see Materials and Methods for details). Clusters were

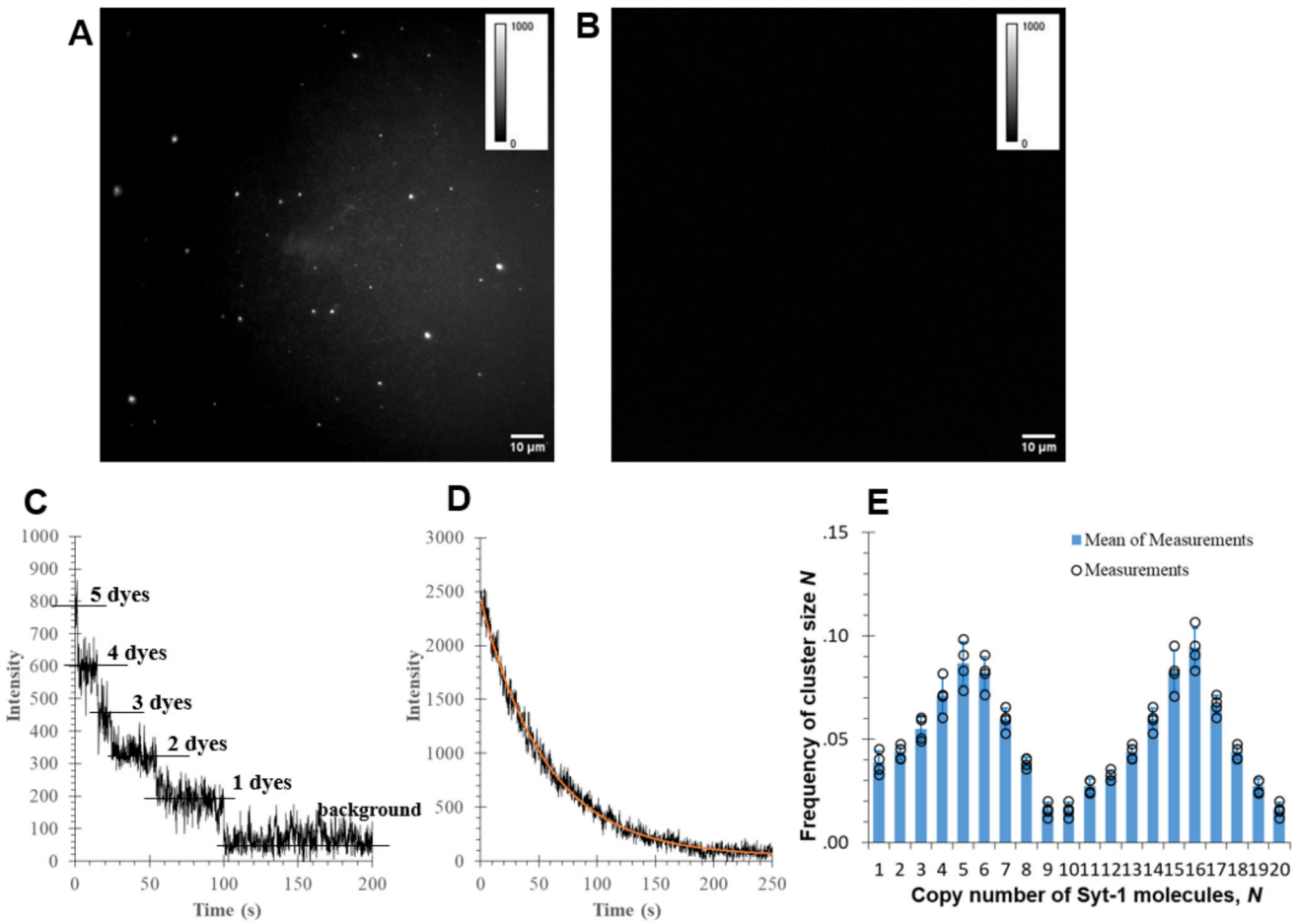

Fig. 1 | Syt-1 forms clusters on lipid bilayer. A DOPC:DOPS:DAG:$PI(4,5)P_2$ (71:25:2:2) bilayer is monitored by TIRF microscopy. **A** When fluorescent wildtype Syt-1 (79–421) is added in solution, protein clusters are observed on the bilayer. A representative image of these clusters is presented here. The buffer is 50 mM HEPES, 140 mM KCl, 10% glycerol, and 1 mM TCEP at pH 7.4. **B** In absence of Syt-1, no fluorescence is observed. **C**, **D** Representative step-bleaching profiles of Syt-1 clusters of different sizes: small cluster (**C**), where the bleaching steps and corresponding numbers of dyes are indicated, and large cluster (**D**), where the bleaching profile displays a smooth decay, which can be fitted with an exponential function (red solid line): $I(t) = I_0 e^{-t/t_0} + B$, where I_0 is the initial intensity at the beginning of bleaching, t_0 is the time constant of bleaching, and B is the background fluorescence. **E** The copy number of Syt-1 in each cluster can be determined by step-bleaching, and from the initial intensity (See Materials and Methods). The distribution of Syt-1 copy numbers in clusters displays a double-peak showing there are two types of clusters ($n = 437$).

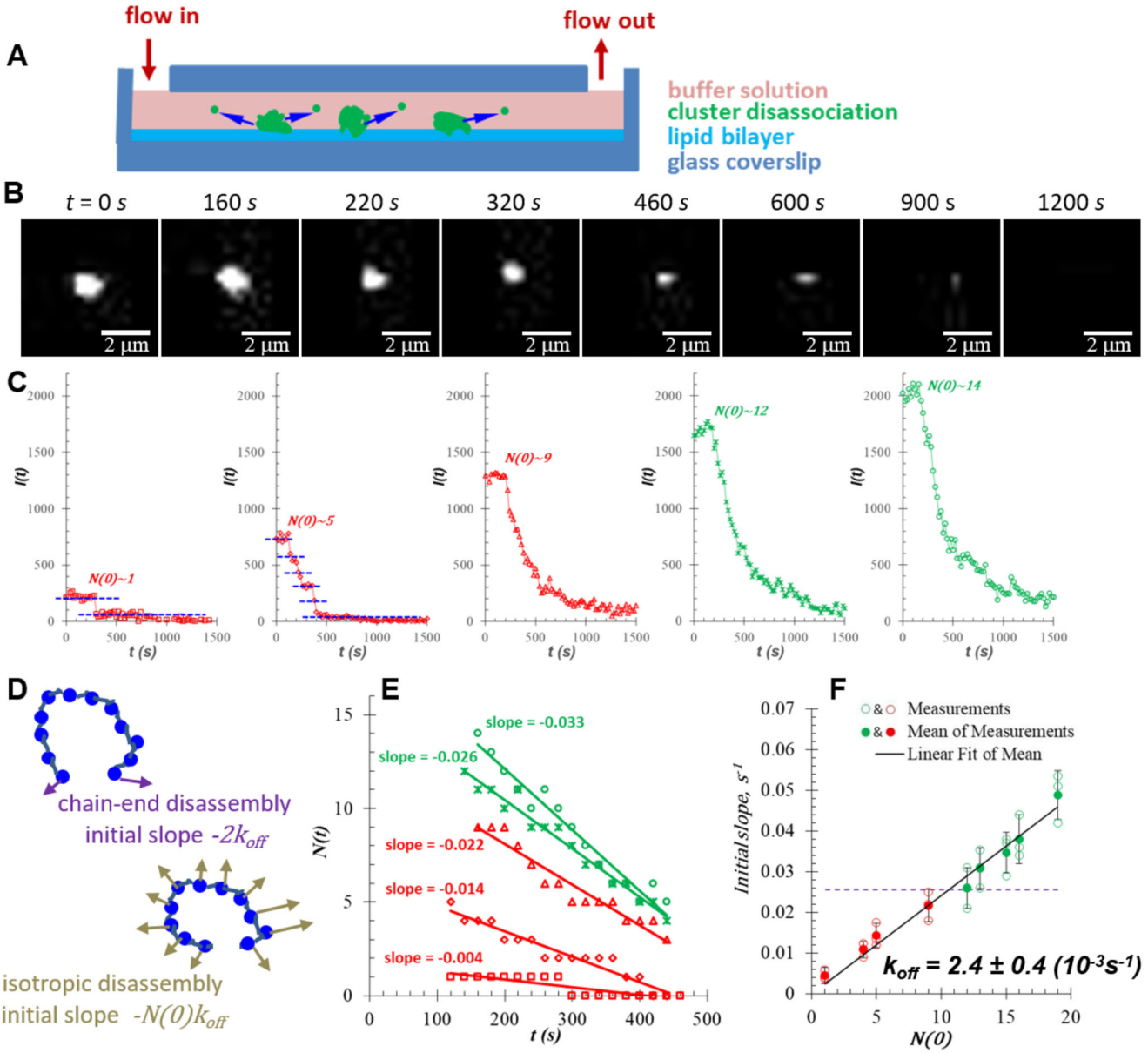

Fig. 2 | Kinetic observation of dissociation of Syt-1 clusters in real-time. **A** Schematic illustration of dissociation of wildtype Syt-1 clusters after flowing in Ca^{2+}-free buffer containing 50 mM HEPES, 140 mM KCl, 10% glycerol, and 1 mM TCEP. **B** Representative TIRF images of the Syt-1 cluster at different time during the process. Dissociation starts at t = 160 s upon the flow of buffer. **C** Representative curves of the fluorescent intensity of Syt-1 clusters versus time showing the dissociation of clusters of different sizes, "small" clusters are in the left three panels (in red) and "large" clusters in the right two panels (green). The blue dashed lines in the left two panels indicate the step-dissociation of small Syt-1 clusters. *N(0)* indicates the estimated initial size of the cluster. **D** Schematic illustration of the two pathways that Syt-1 may utilize for dissociation: the free end disassembly model in which dissociation can only occur at the two ends, and the isotropic internal disassembly model in which every Syt-1 molecule can dissociate from the cluster with equal probability. The initial disassembly slope allows discriminating between the two models. **E** Determination of the slopes of the initial dissociation of the 5 representative clusters shown in (**C**). The intensity, *I(t)*, versus *t* curves were converted into the copy number, *N(t)*, versus *t* curves. (**F**) Determination of unit k_{off} of dissociation of WT Syt-1 clusters. The initial slopes were plotted as function of initial sizes, *N(0)*, and the data were fitted with the free end disassembly model (purple dashed line with $R^2 = 0$) and the isotropic disassembly model (black solid line with $R^2 = 0.98$), respectively. The R^2 values suggests the experimental data is best described by the isotropic internal dissociation process ($n = 27$).

observed on the bilayer membrane (Fig. 1A). As expected, when there was no protein added into the cell, no fluorescent particles were observed lipid bilayer membrane (Fig. 1B).

We first determine the number of copies of Syt-1 in each cluster at equilibrium condition (see Materials and Methods). We gradually bleached the image frames using suitable laser power at different positions. The bleaching profiles of each particle (particle fluorescence intensity versus bleaching time) were plotted. When the protein copy number was small, the bleaching profile displayed apparent discrete steps (Fig. 1C). Then, the actual number of proteins can be determined from counting the number and intensity of steps. When the copy number is large, the bleaching profile becomes smooth and can be fitted with an exponential decay function (Fig. 1D). The size of larger clusters can be calculated from the initial fluorescence intensity of the cluster at the beginning of bleaching divided by the unit intensity of a single fluorophore.

Histograms depicting the observed cluster sizes reveal a broad distribution of copy numbers for Syt-1 molecules, spanning from 1 to 20 molecules (Fig. 1E). This size distribution of the Syt-1 oligomers displays

two distinct populations, which we term small and large. The small clusters contain 5 ± 2 copies of Syt-1, while the large clusters contain 15 ± 2 copies. Previous studies of Syt-1 oligomers by electron microscopy in solution[28] and on lipid monolayers[3] did not report the population of small clusters. However, the size distribution from these studies is similar to the distribution of large oligomers we find here. This consistency in size distribution from results obtained in multiple systems with unrelated methods strongly suggests that the propensity of Syt-1 to form large oligomers is a robust intrinsic property. It is possible that the first class of oligomers was not visualized in the negative staining electron microscopy study, either because their small sizes fell below the detection limit or because they lacked the stability required for the negative staining method.

High-speed atomic force microscopy (HS-AFM) was also used to reveal clusters on lipid bilayers in a similar size range to the large class of oligomers revealed by single molecule counting (See Supplementary Fig. S3). We performed these HS-AFM experiments in part because a previous AFM study[32] also reported ring-like structures. The presence of similar structures in spite of the drastically different experimental conditions (concentration and incubation time) shows the robustness of the Syt-1 cluster formation process. The difference in cluster size, ~150 nm corresponding to 100 or more Syt-1 vs. ~15-mers here, can be explained by the experimental variations. Since there are only 15 to 22 Syt-1 in a synaptic vesicle[34,35], giant clusters with more than a hundred molecules cannot occur physiologically.

Kinetics of disassembly of Syt-1 clusters in real-time

To measure the kinetics of the disassembly of Syt-1 oligomers, we allowed oligomerization to come to equilibrium on a bilayer incubated with solution containing excess Syt-1, and then allowed the system to re-equilibrate once the free Syt-1 was removed. This results in the dissociation of pre-formed clusters.

Therefore, we first prepared a lipid bilayer and mounted the flow cell onto the TIRF microscope. Then we introduced cytosolic Syt-1 solution into the cell. After incubation for 20 min at 23 °C, clusters of wild type Syt-1 formed on the lipid bilayer. Next, a protein-free buffer solution containing 50 mM HEPES, 140 mM KCl, 10% glycerol, and 1 mM TCEP was flowed into the cell at 30 µl/min while the fluorescence of the clusters on the lipid bilayer was monitored in real-time (Fig. 2A). The re-equilibration of the system after removal of the free Syt-1 in solution resulted in the dissociation of pre-formed clusters. The TIRF images of a representative cluster at different time displayed this process (Fig. 2B). Regardless of the varying cluster sizes, all disassembly profiles exhibited a common behavior: initial fluorescent intensities reached a plateau before the buffer's introduction; this plateau was followed by a rapid phase of dissociation of Syt-1 molecules upon the buffer arrival gradually leading to a new plateau of low fluorescent intensities. Fig. 2C shows disassembly versus time profiles separately for the small and large classes of clusters. As expected, in the case of the small clusters we could readily observed single dissociation steps, the intensity decreases between successive steps being approximately the same. Each such step is presumed to represent the dissociation of a single molecule of Syt-1.

As reported before, the oligomers of Syt-1 are likely linear polymers that can close to form rings[3,29]. In principle, the disassembly of such structure may follow either of two distinct mechanisms, either dissociating only at the free ends, or alternatively dissociating from any internal position (Fig. 2D).

In the free end model, the rate of dissociation will be independent of chain length/oligomer size:

$$-\frac{dN(t)}{dt} = 2k_{off} \tag{1}$$

where $N(t)$ is the number of Syt-1 molecules at time t, and k_{off} is the off-rate.

Integrating this equation, we obtain:

$$N(t) = N(0) - 2k_{off}t \text{ or } I(t) = I(0) - 2ak_{off}t \tag{2}$$

where $N(0)$ is the number of Syt-1 molecules before dissociation, $I(t)$ is the intensity of the cluster at time t. $N(t)$ can be converted into $I(t)$ by using $N(t) = I(t)/a$, where a is the unit intensity of a single fluorophore, i.e., the average intensity of a single bleaching step determined using small clusters (see Materials and Methods).

For the internal dissociation model the simplest possibility is isotropic, i.e., every monomer regardless of its position in the oligomer dissociates with equal probability per unit time. Hence, the overall dissociation rate will be proportional to the size of the cluster:

$$-\frac{dN(t)}{dt} = N(t)k_{off} \tag{3}$$

This yields:

$$N(t) = N(0)e^{-k_{off}t} \tag{4}$$

At $t \ll 1/k_{off}$, this equation can be approximated by:

$$N(t) = N(0) - N(0)k_{off}t \text{ or } I(t) = I(0) - I(0)k_{off}t \tag{5}$$

To determine which of these two models best describes our kinetic data, we fitted the initial dissociation slope (initial decreasing of intensity $I(t)$ or copy number $N(t)$ versus t profile) of each individual cluster with a linear function. For instance, in Fig. 2E, we show the initial dissociation slopes of the 5 clusters in Fig. 2C. Then the initial slopes, which are $N(0)k_{off}$, are plotted as function of $N(0)$. Figure 2F shows that these initial dissociation slopes display a linear dependence on $N(0)$ with a substantial slope, suggesting that disassembly of Syt-1 clusters nicely follows the internal (isotropic) disassembly model. In contrast, the horizontal fit (purple dashed line in Fig. 2F) gives an R^2 value of 0, indicating that the experimental data do not follow the free end disassembly model. From the linear fit using the isotropic disassembly model, we obtain a monomer dissociation rate, k_{off}, of $0.0024 \pm 0.0004\ s^{-1}$. The internal model holds for both the small and the large class of Syt-1 clusters (Fig. 2E, F). It is noteworthy that the values of unit k_{off} for the small (5 ± 2) and the large (15 ± 2) clusters were indistinguishable.

Kinetics of assembly of Syt-1 clusters in real-time

We proceeded to investigate the kinetics of the oligomerization process of wild-type Syt-1. A lipid bilayer membrane was made on the glass coverslip of an Ibidi flow cell, which was subsequently mounted onto the TIRF microscope. The microscope was focused on the bilayer, and a solution of Syt-1 in a buffer containing 50 mM HEPES, 140 mM KCl, 10% glycerol and 1 mM TCEP was flowed into the cell at 30 µl/min, all while monitoring the real-time fluorescence of Syt-1 on the lipid bilayer (Fig. 3A).

Upon introduction of the Syt-1 solution, Syt-1 molecules started their association and formed clusters on the lipid bilayer. The TIRF images of a representative cluster at different time points are displayed in Fig. 3B. We analyzed the fluorescent intensity versus time profiles to gain insight into the kinetics of the cluster growth. Figure 3C provides representative growth curves for these Syt-1 clusters, all which shared common features: (1) As expected, no clusters were observed before the introduction of the Syt-1 solution, i.e., the fluorescent intensity remained stable at low, background levels; (2) Rapid association began upon the arrival of Syt-1 and swiftly reached plateaus; and (3) The plateaus were sustained for approximately 10 min before the fluorescent intensities began to slowly decline. Step-like growth was especially notable in the case of small clusters. Intensity increases between neighboring steps are consistent for different cluster sizes. It was noticeable that the addition of Syt-1 molecules to the clusters occurred in a one-by-one pattern.

In light of the bimodal size distribution of Syt-1 clusters (Fig. 1E), we classified all the growth curves into two corresponding categories, slow growth (yielding small clusters) and fast growth (yielding large clusters). The cut-off point was taken to be between 9 and 10 copies of Syt-1 (small being 9 or less, large being 10 or greater). For each class, all the individual curves

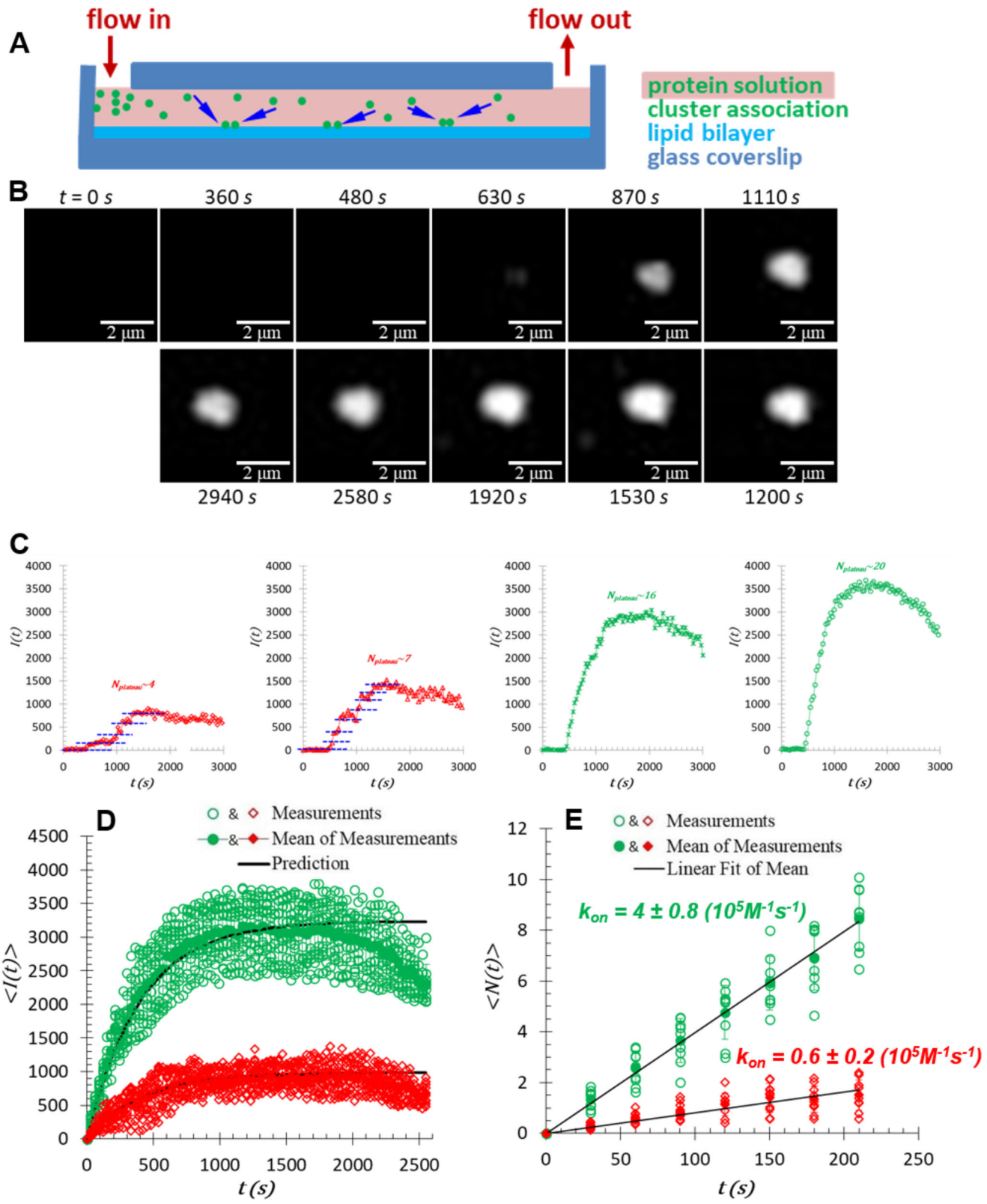

were combined into a single average curve (Fig. 3D, green circles and red diamonds).

To determine the on-rates, k_{on}, from the mean composite growth curves, we considered the initial association of Syt-1 molecules, which follows the equation below:

$$\frac{dN(t)}{dt} = 2k_{on}C \tag{6}$$

Fig. 3 | Kinetic observation of association of Syt-1 clusters in real-time. **A** Schematic illustration of association of wildtype Syt-1 clusters after flowing in Syt-1 solution. **B** Representative TIRF images of the Syt-1 cluster at different time points during the process. Association starts at t = 390 s upon the flow of the protein solution. **C** Representative curves of the fluorescent intensity of Syt-1 versus time showing the association of Syt-1 that grew into clusters of different sizes. The growth of small clusters was marked in red (left two panels), while large clusters in green (right two panels). The blue dashed lines in the left two panels indicate the step-wise association of individual Syt-1 molecules. **D** Averaged growth curves of wildtype Syt-1 cluster and comparison with theoretical predictions. According the bimodal size distribution, all growth curves were divided into two classes with a cutoff between 9 and 10 copies of Syt-1: a slow-growth class that result in small clusters, and a fast-growth class that result in large clusters. In each class, all the curves were averaged into a single one (filled red diamonds and filled green circles; $n = 10$ for small clusters and $n = 9$ for large clusters). Growth predictions (black solid lines) from Eq. 11 of the two averaged growth curves over the whole process, using the two k_{on} from (**E**) and the single k_{off} from dissociation data in Fig. 2F, displayed good matches with the averaged experimental curves. **E** Determination of k_{on} of association of WT Syt-1 clusters on averaged growth curves of the clusters. In each class, k_{on} were obtained from the initial growth of the mean cluster size (filled red diamonds and filled green circles, respectively), $<N(t)>$, versus t curves, which generated a characteristic size, $<N>$, for each class ($n = 10$ for small clusters and $n = 9$ for large clusters).

where C is the concentration of Syt-1. The constant '2' takes into account assembly at each of the 2 free ends of the oligomer. If growth can occur at one end only, as for microtubules or actin, the constant '2' would be removed from Eq. 6 but the rest of the analysis is exactly the same, k_{on} would just be twice larger.

After integration:

$$N(t) = 2k_{on}Ct \tag{7}$$

where $N(t)$ can be calculated through

$$N(t) = \frac{I(t)N_{plateau}}{I_{plateau}} \tag{8}$$

We plotted the initial parts of the two mean composite growth curves (one for the small cluster population and the other for the large cluster population). We fitted them each with the linear functions, respectively, and obtained the two slopes, which are equivalent to $2k_{on}C$.

This enabled us to determine a k_{on} for each cluster class: $k_{on} = (0.6 \pm 0.2) \times 10^5\ M^{-1}s^{-1}$ with a characteristic copy number, $<N_{plateau}> = 4 \pm 1$, for the small cluster class, and $k_{on} = (4 \pm 0.8) \times 10^5\ M^{-1}s^{-1}$ with a characteristic copy number, $<N_{plateau}> = 15 \pm 2$, for the large cluster class (Fig. 3E). These findings suggest that the presence of two distinct cluster populations in the cluster size distribution is a result of the existence of two distinct k_{on} values. Furthermore, it indicates that the size of a cluster is primarily determined at the very outset of cluster formation during the initial association steps, and slow-growing clusters are intrinsically unable to attain the size of large cluster.

The two characteristic copy numbers, $<N_{plateau}> = \sim4$ and ~15, closely align with the two average sizes in the bimodal distribution, namely, $N_{average} = \sim5$ and ~15. The consistency between the copy numbers obtained from the kinetic data and the most probable values from the size distribution shows that these two independent methods converge, thereby confirming the robustness of our findings.

With the measured k_{on} and k_{off} values, it should be possible to predict the entire assembly profiles of Syt-1 clusters at equilibrium, considering the reaction equation:

$$\frac{dN(t)}{dt} = 2k_{on}C - k_{off}N(t) \tag{9}$$

which can be integrated into

$$N(t) = \frac{2k_{on}C}{k_{off}}\left(1 - e^{-k_{off}t}\right) \tag{10}$$

or

$$I(t) = \frac{2k_{on}C}{k_{off}}\frac{I_{plateau}}{N_{plateau}}\left(1 - e^{-k_{off}t}\right) \tag{11}$$

We used Eq. (11), along with the two k_{on} values for the small and large cluster classes, as well as the single unit k_{off} determined from Fig. 2F, to predict the assembly profiles for each cluster classes. In Fig. 3D, the solid black lines represent these predictions for the growth of both cluster classes. Satisfyingly, they closely align with the association phases and plateaus in the experimental data. Equation (11) does not account for the subsequent intensity drops following the plateaus. The underlying mechanism responsible for this decline in fluorescence is unclear but could represent vectorial loss of subunits as rings open and subunits leave before the ring can close again (see Discussion). It is not trivially the result of photobleaching because at the same experimental conditions the cluster fluorescence can remain constant over 1000 s without apparent decrease (Supplementary Fig. S4).

Kinetics of assembly and disassembly of clusters of F349A Syt-1 mutant

The F349A mutant of Syt-1 reduces the interactions between C2B domains[7,29,30]. Negative staining electron microscopy studies revealed that this mutant was not able to form ring-like structures on lipid monolayers[29]. Fusion assays showed that its clamping function was reduced[29,30]. We purified the cytosolic domain (residues 79 to 421) of the Syt-1 F349A mutant (Supplementary Fig. S2). Under the same condition as the wild-type Syt-1, this mutant also formed clusters on lipid bilayers (Fig. 4A), although only the small clusters were observed (Fig. 4B). The peak of large clusters observed with wild-type Syt-1was completely absent in the case of the F349A protein (Fig. 4B). This suggests the interface between neighboring C2B domains in the oligomers is different in large vs small oligomers, and specifically that the inter-subunit interface in large oligomers involves F349, whereas the interface in small oligomers does not require this residue.

We also monitored the disassembly process of the small Syt-1 F349A clusters when equilibrium was abruptly perturbed by removing the protein from the medium. Supplementary Fig. S5 presents representative fluorescent intensity profiles over time. We fitted the initial dissociation phase of each individual F349A cluster the same as for the wild-type Syt-1, with a linear function thereby determining the initial slope for each individual cluster (Supplementary Fig. S6). These slopes, representing $N(0)k_{off}$, were plotted as function of $N(0)$ (Fig. 4C). Like wild-type Syt-1, the slopes of initial dissociation phase were linearly related to $N(0)$, indicating that the disassembly of Syt-1 F349A clusters also follows the internal, isotropic disassembly mechanism. We then determined the unit off-rate for the F349A mutant $k_{off} = 0.0017 \pm 0.0003\ s^{-1}$, which is indistinguishable from the off-rate of the wild-type Syt-1 clusters ($0.0024 \pm 0.0004\ s^{-1}$).

We also monitored the assembly process of Syt-1 F349A clusters by analyzing fluorescence intensity profiles over time. Supplementary Fig. S7 shows representative growth curves of these mutant clusters which all have similar features: cluster growth initiated promptly when the mutant protein solution arrived, gradually reaching plateaus, followed by a slow decrease in the fluorescence intensities. This process yielded steady-state small clusters of varying sizes, often characterized by step-like growth.

We then averaged all the growth curves into a single composite one (Fig. 4D, red diamonds). The initial segment of this averaged growth curve was plotted and fitted with a linear function (Fig. 4E), yielding a slope $2k_{on}C$ and a value for k_{on} for the assembly of the F349A clusters of $(0.4 \pm 0.1) \times 10^5\ M^{-1}s^{-1}$ with a characteristic copy number, $<N_{plateau}> = 4 \pm 1$. Notably, this on-rate is similar to the on-rate of the assembly of

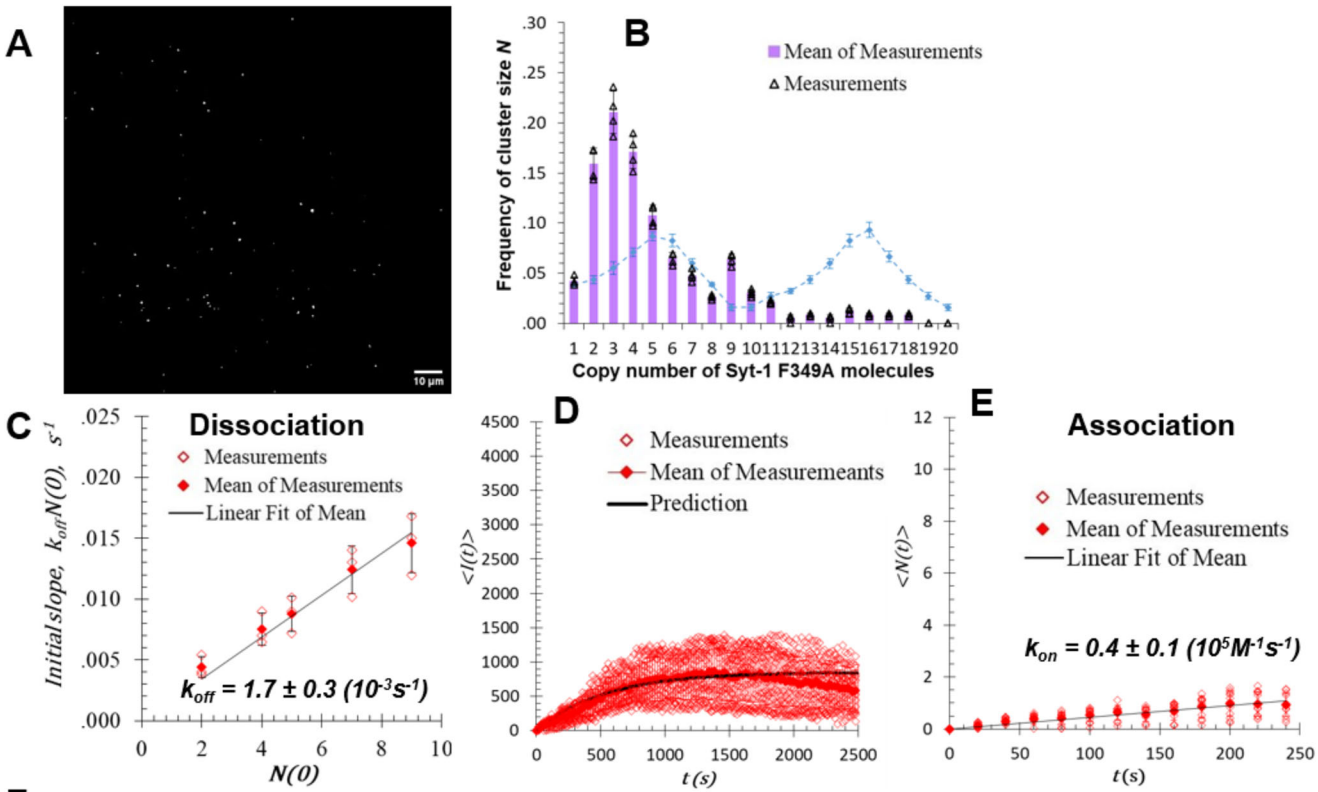

F

	# of peaks in distribution	k_{off} (10^{-3} s^{-1})	<N>	k_{on} (10^5 s^{-1} M^{-1})	K_D (nM)	surface density (protein per μm²)
Wildtype	2	2.4 ± 0.4	4	0.6 ± 0.2	40 ± 8	0.08 ± 0.02
			15	4 ± 0.8	6 ± 2	
F349A	1	1.7 ± 0.3	4	0.4 ± 0.1	45 ± 15	0.04 ± 0.01

Fig. 4 | Kinetic observation of dissociation and association of the clusters of the Syt-1F349A clamping mutant in real-time. A Representative TIRF image of clusters formed with Syt-1 mutant F349A mutant. **B** The copy number of Syt-1 F349A mutant in each cluster can be determined by step-bleaching, and from the initial intensity. The distribution of copy numbers of Syt-1 F349A clusters displays a single-peak with small cluster size ($n = 573$). The blue dashed line represents the distribution of wildtype Syt-1 clusters, which serves as a reference. **C** Determination of unit k_{off} for dissociation of Syt-1 F349A clusters. The initial dissociation slopes were plotted as function of initial sizes, $N(0)$, and displayed a proportional relationship ($n = 15$). **D** Averaged growth curves of Syt-1 F349A cluster and comparison with theoretical predictions. All the curves were averaged into a single one (filled red diamonds; $n = 12$). Growth predictions (black solid line) from Eq. 11 of the averaged growth curves over the whole process, using the k_{on} from (**E**) and the k_{off} from dissociation data in (**C**), displayed good matches with the averaged experimental curves. **E** The initial slope of the averaged growth curve of Syt-1 F349A clusters allows the determination of k_{on} for the formation of Syt-1 F349A clusters (same as Fig. 3E) ($n = 12$). **F** Summary of kinetic and thermodynamic parameters of the oligomerization of wild-type (WT) Syt-1 and the F349A mutant ($n = 4$ for surface densities).

wildtype Syt-1 into small clusters $(0.6 \pm 0.2) \times 10^5\ M^{-1}s^{-1}$, but significantly slower than the assembly kinetics of large clusters $(4.0 \pm 0.8) \times 10^5\ M^{-1}s^{-1}$.

To test the self-consistency of the entire data set, we used the kinetic parameters to predict the steady-state cluster size distributions and growth curves for the F349 mutant clusters, employing Eq. (11) and utilizing k_{on} and k_{off} as determined from Fig. 4C, E, respectively. The solid black line in Fig. 4D represents these predictions for the growth of the clusters, providing a good match with the observed association phases and plateaus.

The subunit binding constant, K_D, can be calculated from the ratio $K_D = k_{off}/k_{on}$. The binding constants for the two populations of wild-type Syt-1 clusters were 6 ± 2 nM for the large clusters, and 40 ± 8 nM for the small clusters (Fig. 4F). For comparison, it is worth noting that the subunit binding constant of wild-type Syt-1 oligomerization in solution in the presence of Mg^{2+} and ATP was estimated using FCS to be ~1 μM[28]. The better affinity we find here suggests that the oligomers are more stable on lipid bilayer than in solution.

The binding constant of the small (and only class of) F349A oligomers was 45 ± 15 nM, indistinguishable from the ~40 nM for the small wild-type clusters. This reinforces our earlier conclusion that F349 contributes binding energy to the packing of C2B domains in the large but not the small oligomer class. Because F349A reduces vesicle clamping, this suggests that clamping involves large oligomers and not small oligomers.

Kinetics of dissociation of Syt-1 clusters in the presence of Ca^{2+}

In the previous experiments, we determined that the off-rate of wild-type Synaptotagmin -1 clusters in Ca^{2+}-free buffer was approximately 0.0024 s^{-1}. This demonstrated that these cluster had a lifetime of around 1000 s in the absence of Ca^{2+}. However Ca^{2+}-evoked neurotransmitter release occurs

rapidly, so it is essential to investigate the kinetics of cluster dissociation in the presence of a Ca^{2+}-containing buffer.

Following the same procedure as before, we allowed Syt-1 clusters to assemble to equilibrium on a lipid bilayer membrane and then added 1 mM $CaCl_2$, which was flowed into the cell at 30 µl/min. The fluorescence intensity of each cluster was measured in real-time. The vast majority of clusters, both small and large, underwent rapid dissociation and diffused away within a single image frame. Figure 5A provides a series of frame-by-frame images for five representative clusters. The Ca^{2+} arrived between frames 3 and 4 as confirmed by the sharp decrease in background fluorescence (Fig. 5B). The sharp decrease in background fluorescence was due to the flow of non-fluorescent buffer which suddenly diluted and eventually replaced the original incubating buffer that contained fluorescent Syt-1. At this time point of dissociation, the effective Ca^{2+} concentration was diluted to about 200 µM.

The top two panels depict the dissociation of small clusters, while the three bottom panels depict the dissociation of large clusters. An intriguing observation was the ability to capture the moment that when clusters disintegrated explosively and dispersed in all directions from their original position (Cluster #5, frame 4, Fig. 5A). The time interval between consecutive image frames was 4 s. Figure 5B represents profiles of decreasing fluorescent intensities of background and clusters of different sizes (left panel: small cluster; right panel: large cluster) during the buffer flow with Ca^{2+}. The sudden decrease in fluorescence usually occurred at a single video frame simultaneously for both background and clusters, suggesting that Syt-1 clusters disassemble faster than the temporal resolution limit of the experiment.

In previous experiments, we found that spontaneous dissociation of Syt-1 oligomers (in the absence of Ca^{2+}) followed the internal, isotropic disassembly model. This model also fits well with our observation in the presence of Ca^{2+}, where all the monomeric units in the oligomer "explode" and move out along all directions.

The disappearance of the Syt-1 clusters with calcium could also be observed by HS-AFM (Fig. 6A, B).

Old and new clusters remain distinct

We used two-colors of Syt-1 to simultaneously monitor the de novo assembly of new Syt-1 clusters in the presence of "old" pre-existing clusters. To do this, we first prepared the lipid bilayer on the glass coverslip and added "old" Syt-1 Alexa-488. After an incubation period of 20 min, a solution containing "new" Syt-1 Alexa-647 was then flowed into the cell, as illustrated in Fig. 7A. The fluorescence of Alexa-488 and Alexa-647 were both measured in clusters over time. Figure 7B displays representative TIRF images of both channels vs. time. In the top panel, clusters of Syt-1 labeled with Alexa-488 gradually dissociated, while, in the bottom panel, Syt-1 labeled with Alexa-647 gradually assembled into new oligomers at distinct locations. Interestingly, no "new" Syt-1 Alexa-647 molecules were added into the pre-existing "old" Syt-1 Alexa-488 oligomers, even though they were already largely dissociated.

Discussion

Syt-1 clusters represent polymerized monomers

Four lines of evidence establish that the clusters of Syt-1 observed to assemble on lipid bilayers are due to oligomeric self-assembly of Syt-1 into polymers, as distinct from happenstance occupancy of the same limited region of the bilayer surface, in spite of the spatial limits of optical microscopy (~300 nm). First, the bimodal size distribution observed (Fig. 1E) in no way matches the simple Poisson distribution expected for random clustering at the same overall surface density (Supplementary Fig. S8). Second, the consistent growth of each cluster from an initial seed (Fig. 3C) independently rules out resolution artefacts. Third, the near elimination of the large clusters (Fig. 4B) by point mutation (F349A) establishes a direct interaction between subunits involving the mutated C2B domain. Finally, the clusters are not entirely immobile on the lipid bilayer surface. The lateral movements of the clusters on the bilayer surface reveal a standard diffusion of the clusters with a diffusion coefficient that decreases with the cluster size (See Supplementary Fig. S9). Hence, the colocalized Syt-1 molecules actually belong to a single entity and the clusters are actually Syt-1 oligomers.

Nucleation of Syt-1 oligomers

We observed a bimodal size distribution of the oligomers, with average copy numbers around 4 (small clusters) and 15 (large clusters), respectively. The small and large clusters have similar off-rate (unit k_{off}), however, the association rate is about 6 times slower for small clusters compared to large clusters. Hence, the size difference in the small and large clusters is the consequence of the distinct growth kinetics.

The sizes of small and large classes of oligomers is determined by the differing association rates of their Syt-1 subunits. Intriguingly, in Fig. 3D, E, the increase in oligomer size exhibits a linear progression right from the initiation of the oligomerization process. This linear growth, faster for the larger oligomers than for the smaller ones, suggests that, even at the first moment when the smallest Syt-1 oligomer forms, the fate of the oligomer (large vs small) has already been determined. This suggests that the small and large oligomers are nucleated by distinct "seeds", the large seed involving residue F349 and the small seed not. Since the two peaks in Fig. 1E contain approximately equal numbers of oligomers, it appears that the two molecular seeds responsible for driving oligomer formation are equally probable and thus energetically similar.

Molecular organization and kinetics of Syt-1 oligomers

The observation that the spontaneous dissociation rate at equilibrium is linearly related to oligomer size (Fig. 2F) implies the absence of end effects, and shows that all Syt-1 molecules in the oligomer are identically arranged in a closed structure. This observation indicates that the valency of Syt oligomers is 2, meaning each Syt-1 can only bind two other Syt-1, generating a linear oligomer. Indeed, if the valency was 3 or more, each Syt-1 could bind at least 3 other Syt-1 molecules and the cluster would look like a network that would be almost impossible to lock at a finite size in a two-dimensional context. Conversely, a linear oligomer can loop on itself, like a ring. Hence, our results suggest that the closed structure we observe is a closed ring topology.

Previously, Syt-1 rings composed of 11 to 26 (16 ± 4) copies were observed to spontaneously form on phospholipid monolayers[3] or in solution[28]. Our current findings now confirm that similar ring oligomers also can assemble on phospholipid bilayers, with the size of the larger class of oligomers aligning with previously reported observations. The smaller oligomers might not have been detected earlier, possibly due to their insufficient contrast for visualization by negative-staining electron microscopy. According to our model, the ring-like structure remains stable during disassembly, but the ring dimensions decrease as Syt-1 molecules detach from the oligomer.

In summary, we propose the following scenario (Fig. 8). Initially, linear oligomers nucleate from one of two possible distinct initial "seed" conformations which dictates whether they will ultimately grow to be small or large oligomers (phase I). As the oligomers grow (phase II), they reach an equilibrium size determined by their rates of association and dissociation (phase III). The positions of the linear oligomer ends fluctuate over time, and during this movement, the two ends eventually meet and bind (phase IV). This event locks the oligomer in place, forming a ring-like structure that can no longer add subunits to grow. When a Syt-1 molecule dissociates from the oligomer, the ring is opened and it is possible that other Syt-1 may bind to the two loose ends thereby increasing the oligomer size. Alternately, the two loose ends, already very close to each other may meet and reseal the ring before any other free Syt-1 can bind to one end. In the two-color experiment presented in Fig. 7, the pre-existing Syt-1 Alexa-488 oligomers have been formed for more than 20 minutes. When the flow of Syt-1 Alexa-647 solution arrives, these Syt-1 Alexa-488 oligomers have already passed Phase IV (not in Phase III anymore), i.e., locked in a ring-like structure. The new coming Syt-1 Alexa-647 cannot insert within these already existing locked Syt-1 Alexa-488 clusters and can only form new pure Syt-1 Alexa-647

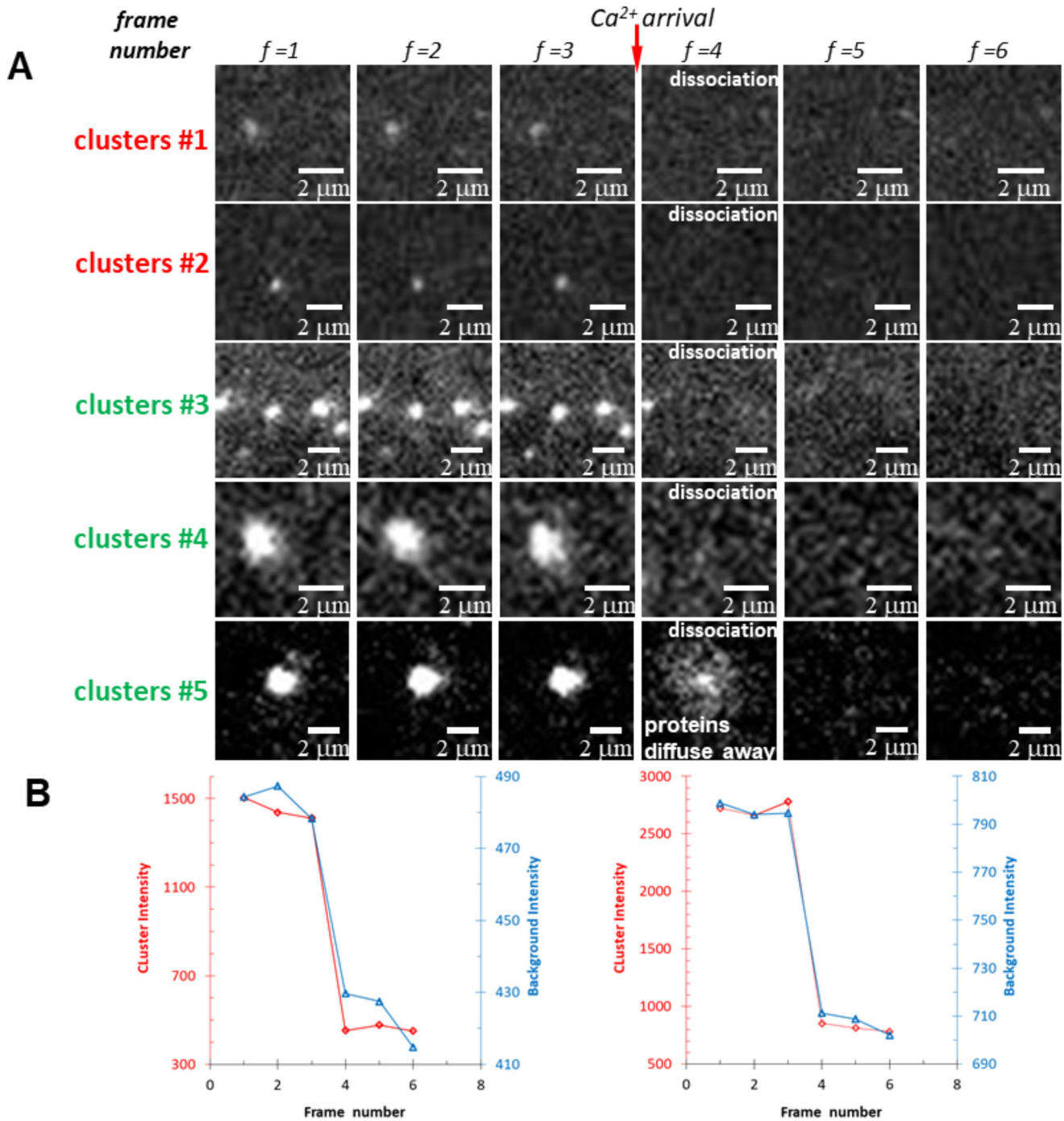

Fig. 5 | Kinetic observation of dissociation of Syt-1 clusters in the presence of Ca^{2+} in real-time. A Frame-by-frame displays of the dissociation of Syt-1 clusters after flowing in Ca^{2+}-containing buffer. Most clusters, including small (clusters #1 and #2) and large ones (#3, #4, and #5), dissociated in one image frame ($n = 4$). The interval between neighboring frames was 4 s. **B** Representative curves of the fluorescent intensity of Syt-1 clusters (red diamonds) or background (blue triangles) versus time showing the rapid dissociation of clusters of different sizes (left panel: small cluster; right panel: large cluster) simultaneously upon the entry of flow of Ca^{2+}-containing buffer. The sharp decrease in background fluorescence was due to the flow of non-fluorescent buffer which diluted and replaced the original incubating buffer that contained fluorescent Syt-1.

clusters, indicating that ring resealing is faster than addition of new Syt-1 to the loose ends. Hence, once the oligomer is locked in a ring-like structure (phase IV), it can only decrease in size (phase V).

Syt-1 oligomers have sufficient stability to function as fusion clamps

Synaptic vesicles docked and primed for ready-release at presynaptic terminals must generally await a signal to secrete their neurotransmitter in order to pass information from action potentials synchronously across synapses. Specifically, entering Ca^{2+} ions (permitted by the opening of nearby voltage-gated channels) trigger fusion by binding to Syt-1, releasing its clamp on SNARE-mediated vesicle fusion[17]. In our models[36,37] ring oligomers of Syt-1 are critical for the stability of the fusion clamp because they radially restrain SNAREpins from zippering to completion. The loss or reduction in clamping when the large class of oligomers are eliminated by the F349A mutation[25,29,30] provides strong evidence for this model. Also,

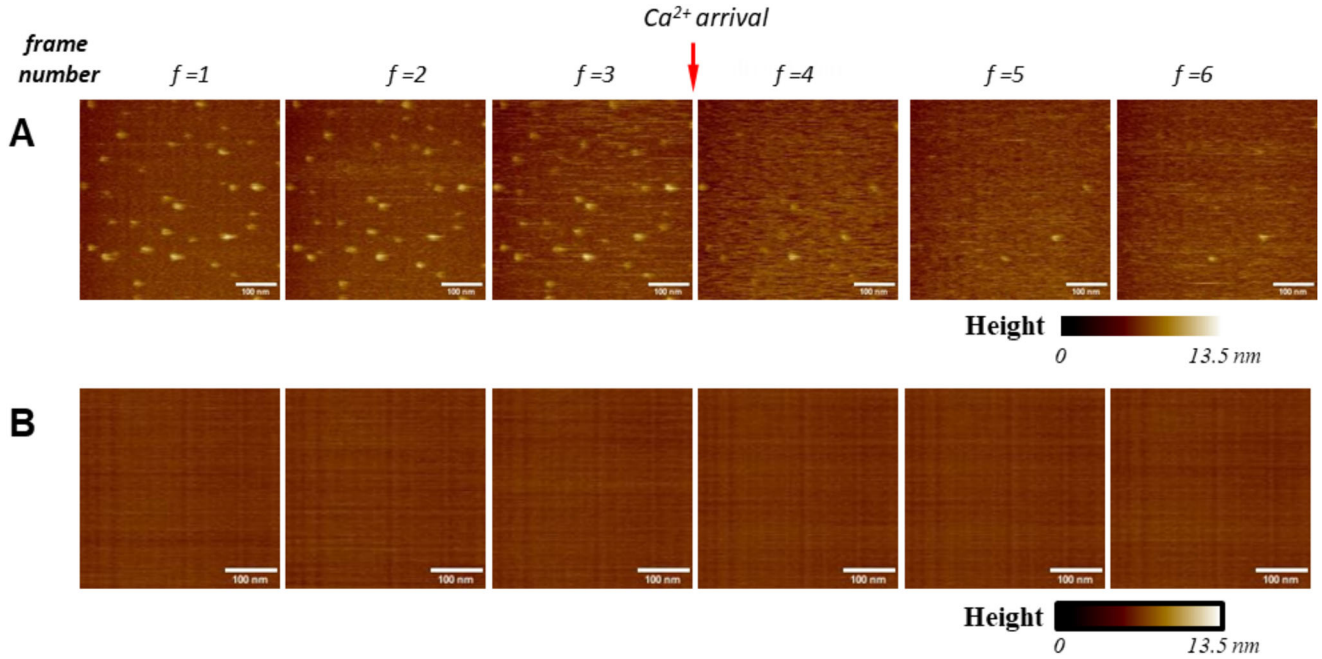

Fig. 6 | High Speed Atomic Force Microscope (HS-AFM) imaging of disassembly of Syt-1 clusters in the presence of Ca^{2+} in real-time. A Frame-by-frame displays of the dissociation of Syt-1 clusters upon flowing in Ca^{2+}-containing buffer. Most clusters dissociated in one image frame. The interval between neighboring frames was 1 s. **B** Frame-by-frame displays of the AFM images of the lipid bilayer in the absence of Syt-1 upon flowing in Ca^{2+}-containing buffer.

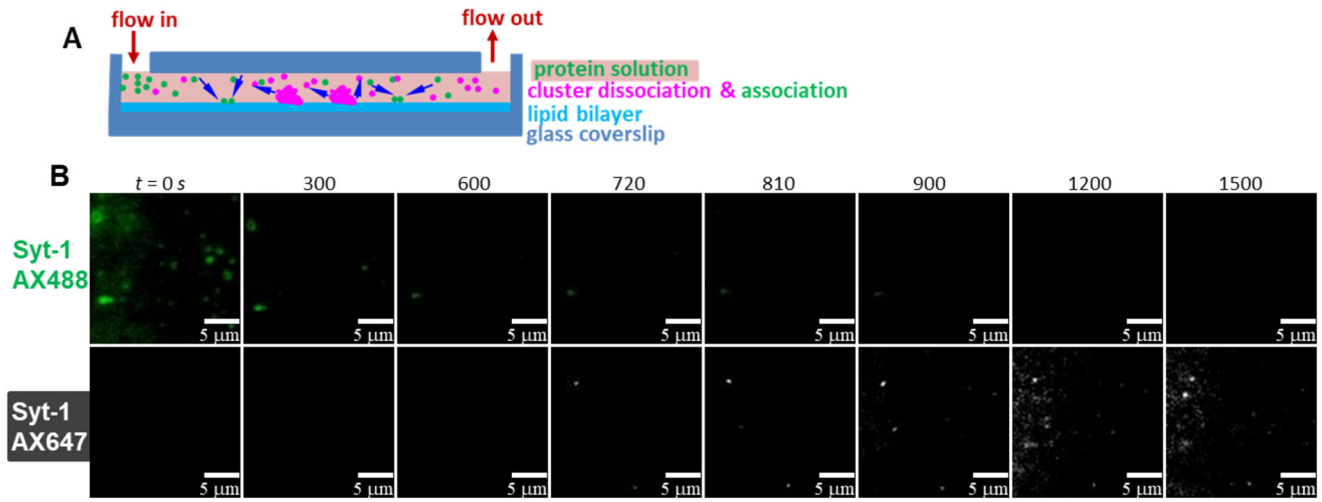

Fig. 7 | Monitoring association and disassociation of two colors of Syt-1 clusters simultaneously. A Schematic illustration of dissociation of wildtype Syt-1 Alexa488 clusters and formation of wildtype Syt-1 Alexa647 clusters. Syt-1 Alexa488 clusters on lipid bilayer were pre-formed by incubating with Syt-1 Alexa488 solution. Then Syt-1 Alexa647 solution flowed in. **B** Representative TIRF images of Syt-1 Alexa 488 clusters (top panel, green), and Syt-1 Alexa647 clusters (bottom panel, white), at different time. The two panels showed the same area on the lipid bilayer. Growth of new clusters usually occurred at a fresh spot ($n = 3$).

since clusters of F349A have similar off-rate and on-rate as the small clusters of the wild-type Syt-1, the main clamping function is probably fulfilled by the large clusters of wild-type Syt-1.

Certain quantitative physical-chemical properties of Syt-1 oligomers are required for the model to be tenable. Satisfyingly, the quantitative kinetic data reported here so far meet all the following requirements for a steric clamp in the process of synaptic vesicle fusion:

1. *Rapid assembly*: The clamp must swiftly form between the vesicle and membrane when needed within the time frame physiologically available for vesicle priming.
2. *Robustness and durability*: The clamp must be robust and durable, being stable long enough to explain the observed rates of spontaneous vesicle release in synapses.
3. *Near instantaneous dismantling*: The clamp must dissociate within the time frame of synchronous neurotransmitter release of < 1 ms.

The on-rate for Syt-1 oligomer formation is approximately $4 \times 10^5\ M^{-1}s^{-1}$. The number of Syt-1 molecules per synaptic vesicle is 15–22[34,35]. Hence in the volume between docked vesicle and plasma membrane, the concentration of Syt-1 is in between 1 and 10 mM[38]. Thus $k_{on}C$ is between 300 and 3000 s^{-1} and the time needed to form oligomers between vesicle membrane and presynaptic terminal is around 0.3–3 ms. The time required for docking and priming of synaptic vesicles at the plasma membrane of fast synapses is ~100 ms[39], so an effective clamp must assemble within this time frame. Our quantitative data reveal that the rapid formation of Syt-1 oligomers fits requirement 1 for rapid formation of the clamp.

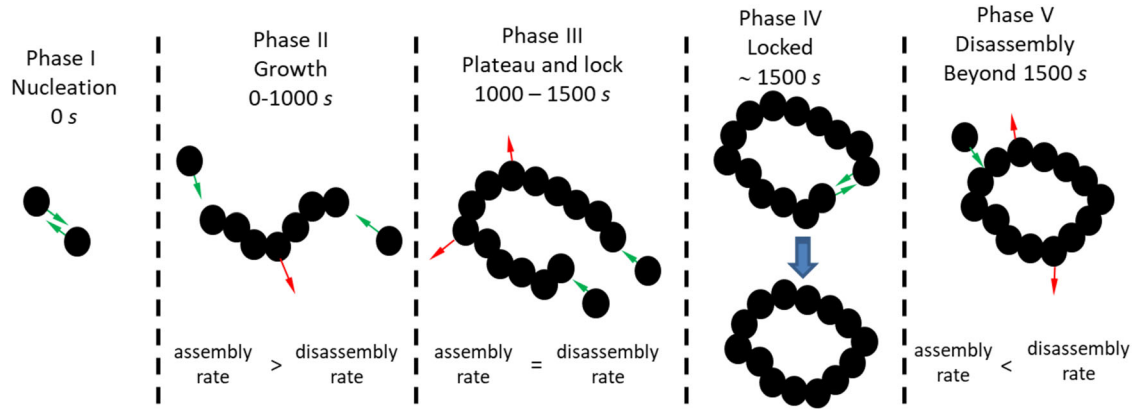

Fig. 8 | Model of successive phases in the assembly/disassembly of Synaptotagmin oligomers. This model provides an explanation for the observed kinetics of Syt-1 oligomers, as presented in Fig. 3D. Based on experimental observations, the key assumptions are as follows: i. the oligomer exhibits a linear structure; ii. Additional Syt-1 primarily binds through the two ends of the oligomer; iii. All Syt-1 can dissociate from the oligomer at a rate independent of their location, and the oligomer reseals after a Syt-1 dissociates. I) Nucleation: At time 0, a first Syt-1 dimer assembles, initiating the nucleation of the Syt-1 oligomer. This nucleation seed can have two forms that determine the assembly rate of the subsequent Syt-1. The slower (resp. faster) assembly rate will lead to the smaller (resp. larger) oligomers; II) Continuous Growth: Following nucleation, the low number of Syt-1 molecules in the oligomer results in an assembly rate exceeding the disassembly rate. Hence, the oligomer experiences continuous growth due to the addition of new Syt-1; III) Plateau Phase: As the oligomer size increases, the disassembly rate eventually matches the assembly rate. Despite ongoing addition and dissociation of Syt-1, a steady state is reached and the oligomer size remains constant during this plateau phase; IV) Loop Formation: During the plateau phase, the two Syt-1 molecules at the end of the monomer eventually meet in their fluctuating movement and bind. This binding locks the oligomer in a loop; and, finally V) Size Reduction: Once the oligomer is locked, dissociation can still occur, but binding of new Syt-1 is restricted. Consequently, the oligomer size decreases during this phase.

The proposed Syt-1 ring clamp's intrinsic nature involves utilizing its molecular volume to maintain spacing between the docked vesicle and plasma membrane and restrain bound SNAREpins, reducing premature spontaneous fusion. Our quantitative data also bear on the potential stability of a ring-based Syt-1 clamp (requirement 2). Specifically, for a given dissociation rate, k_{off}, the lifetime of an oligomer of initial size $N_{\max}$ is: $\sum_{n=3}^{N_{\max}} \frac{1}{nk_{off}}$. Each term in the sum corresponds to the dissociation of one Syt-1 from the oligomer. Since large Syt-1 oligomers have an intrinsic (in the absence of Ca^{2+}) dissociation rate of about $k_{off} = 0.0024\ s^{-1}$ their lifetime is approximately 1000 s. This extended lifetime allows for the accumulation of enough vesicles and precise configuration of accessory proteins, crucial for synchronized fusion.

In contrast, for the oligomers of the F349A mutant of Syt-1, although the off-rate is similar, however, due to their small copy number, they can last around 100 *s* between the vesicle and the plasma membrane. Therefore, the wild-type Syt-1 oligomer is able to hold clamping sufficiently long for evoked fusion, fulfilling requirement 2 for the stability of the clamp, while the F349A mutant oligomers have much shorter lifetime, hence they are not able to effectively reduce spontaneous fusion. These results are consistent with in vivo and in vitro functional assays[25,29,30].

Finally, in neurotransmission, the rate of fusion is in the sub-millisecond range upon the entry of Ca^{2+} flow. Thus the clamp must vanish in this time scale. Our study reveals that Syt-1 oligomers disassemble themselves and disperse within a single image frame in both TIRF and HS-AFM experiments, approximately 1 *s*, satisfying the requirement for the clamp to vanish upon Ca^{2+} entry. We suspect that the Syt-1 oligomers dissociate much faster than this when they encounter Ca^{2+}, but future experiments with far better time resolution will be needed to test requirement 3 further.

Materials and Methods

Chemicals

4-(2-Hydroxyethyl)piperazine-1-ethanesulfonic acid (HEPES), Potassium hydroxide (KOH), Potassium chloride (KCl), Magnesium chloride ($MgCl_2$), Calcium chloride ($CaCl_2$), Glycerol, DNAse I, RNAse A, Benzonase, Roche complete protease inhibitor cocktail tablets, and DL-Dithiothreitol (DTT) were purchased from Sigma-Aldrich. Nickel-NTA agarose, TCEP-HCl were supplied by Thermo Fisher Scientific. The lipids used in this study, 1,2-dioleoyl-sn-glycero-3-phosphocholine (DOPC), 1-palmitoyl-2-oleoyl-sn-glycero-3-phosphocholine (POPC), 1,2-dioleoyl-sn-glycero-3-(phospho-L-serine) (sodium salt) (DOPS), L-α-phosphatidylinositol-4,5-bisphosphate (Brain, Porcine) (ammonium salt) (brain $PI(4,5)P_2$), and 1-2-dioleoyl-sn-glycerol (DAG) were purchased from Avanti Polar Lipids. Alexa Fluor® 488 Maleimide and Alexa Fluor® 647 Maleimide were purchased from Thermo Fisher Scientific. SUMO protease was home purified. All aqueous solutions were prepared using 18.2 MΩ ultra-pure water (purified with the Millipore MilliQ system).

Protein constructs, expression and purification

We elected to work with Syt-1 constructs that do not contain the transmembrane domain because previous studies showed that (i) Syt-1 ring formation seems to be due to the C2B domain[7], and (ii) the disordered region following the transmembrane domain provides enough orientational freedom for the C2B domain to bind opposing membranes through the polybasic patch[40,41]. Hence, the transmembrane domain is unlikely to affect oligomerization.

The vector expressing the cytosolic domain of Syt-1, residues 79 to 421, was cloned from rat Synaptotagmon-1 to a pET28 plasmid. A His_6-SUMO tag was inserted into the vector, right before the N-terminus of the Syt-1 aa. 79 to 421 (Supplementary Fig. S1), similarly to previous report[38]. To ensure a single Cysteine residue on position 79, Cysteine residues at position 82 and 277 were mutated into Serine and Alanine residues respectively.

This plasmid was used as a template to generate the Syt-1 F349A mutant using a QuickChange mutagenesis kit (Agilent Technologies as before[16]).

The cytosolic Syt-1 and Syt-1 F349A mutant were expressed in bacterium cells, BL-21 gold (DE3) Escherichia coli bacterial strain. Similarly to previous report[38], a 4 *L* culture of this bacteria grown at 0.6–0.8 OD (600 nm) cell density was induced with 0.5 mM Isopropyl-β-D-thiogalactopyranoside (IPTG) for 4 h at 37 °C. Cells were pelleted.

The Syt-1 proteins were then purified using Ni-NTA affinity beads as described before[33,38,42]. To summarize, the cell pellet was thawed on ice and resuspended in 50 ml buffer containing 50 mM HEPES (pH 7.4), 400 mM KCl, 10% Glycerol (w/v), 1 mM TCEP, 0.5 mM of phenylmethanesulfonylfluoride (PMSF), 10 µg/ml DNAse I, 10 µg/ml RNAse A, 10 µl Benzonase, and 1 tablet of EDTA-free protease inhibitor cocktail (Roche). Triton X-100 was then added to the suspension to a final concentration of 4% (v/v). This

suspension was passed 4 times through the French press cell disruptor. The lysate was centrifuged at 40,000 rpm in a Ti45 rotor (Beckman) for 40 min at 4 °C. The supernatant was removed and 2 ml Qiagen Ni-NTA slurry along with 10 ul Benzonase were added, and subsequently rotated using an orbiting wheel overnight at 4 °C. The beads were washed at 4 °C with 30 ml buffer containing 50 mM HEPES at pH 7.4, 400 mM KCl, 10% glycerol, 1 mM TCEP, and 10 mM Imidazole, then with another 30 ml buffer containing 50 mM HEPES at pH 7.4, 400 mM KCl, 10% glycerol, 1 mM TCEP, and 25 mM Imidazole, followed the third 30 ml buffer containing 50 mM HEPES at pH 7.4, 270 mM KCl, 10% glycerol, 1 mM TCEP, and 25 mM Imidazole. 100 µl of SUMO protease (~2 mg/ml) in 1 ml buffer was added to the beads and incubated for 3 h at room temperature with shaking to remove the 6xHis SUMO tag while bound to the Nickel-NTA column.

After the cleavage reaction, elusions were collected. To remove RNA/DNA contamination during purification of Syt-1, the eluted protein was further purified by using the AKTA with a MonoS cation exchange column and a 10 ml superloop. To clean the MonoS column, 10 ml 0.5 M NaOH was first injected into the superloop and flowed into the MonoS column in the reversed position (upside down). Then 5 ml 1 mg/ml pepsin enzyme was injected into the superloop and flowed into the MonoS column. The MonoS column was then detached from the AKTA and both ends were sealed. Digestion was performed in a 37 °C incubator for 1 hour. After digestion, 10 ml 0.5 M NaOH was injected into the superloop and flowed into the MonoS column in the reversed position again. The MonoS column was then put in upright position, and washed by 10 ml low salt buffer A (50 mM HEPES, 0 mM KCl, 20% glycerol, 1 mM TCEP), then by 10 ml 100% buffer B (50 mM HEPES, 2000 mM KCl, 20% glycerol, 1 mM TCEP), and finally by 5% B. The flow running through MonoS column was kept continuously at 0.5 ml/min with 5% B. Then superloop was washed with 10 ml water. When the column was ready, dilute the Syt-1 protein until 100 mM KCl in the buffer is reached, and inject it to the superloop, and flow into the MonoS column. This would allow Syt-1 to bind the column at 100 mM KCl. After the binding reached steady state (the conductivity curve became flat), set Gradient to "100% B, length = 60 min". The KCl concentration would increase gradually and the Syt-1 protein would be eluted.

SDS-gel electrophoresis and UV absorption analysis showed that the fraction eluted from MonoS column at about 700 mM KCl was pure and had a ratio of absorption at 260 nm over 280 nm smaller than 0.6, which indicated that it was RNA/DNA-free (Supplementary Fig. S2). The protein concentration was typically 1 mg/ml as determined by using a Bradford protein assay and/or Nanodrop 2000.

Protein labeling

We learned that the N-terminal Cysteine residue was more efficient in the coupling reaction with a maleimide fluorescent dye. Hence we used the native Cysteine residue at position 79 of Syt-1 for labeling with the maleimide-AlexaFluor 488 or AlexaFluor 647. All other Cysteine residues were mutated to Serine or Alanine.

The cytosolic Syt-1 and its F349A mutant were labeled by incubating the proteins with Alexa 488 or Alexa 647 conjugated with a Maleimide group from Thermo Fisher Scientific, as described before[33]. The protein was first centrifuged at 14,000 rpm for 20 min at 4 °C to remove any precipitation. Fluorescence dye was added into the protein solution at dye:protein = 5:1 molar ratio and the mixture was incubated for 30 min at room temperature with gentle rotation. Unreacted dye was removed by passing through the illustra NAP-5 and NAP-10 (Cytiva GE Healthcare) three times at room temperature.

The labeling efficiencies of WT Syt-1 and the F349A mutant are close to 95%. More specifically, WT Syt-1 with Alexa 488 around 95%, WT Syt-1 with Alexa 647 around 97%, F349A mutant with Alexa 488 around 94%, F349A mutant with Alexa 647 around 98%, respectively.

Liposome formation

Protein-free liposomes were prepared by extrusion using an Avestin mini-extruder[8,16]. To make the liposomes for preparing bilayers, DOPC, DOPS, DAG, and PI(4,5)P_2 were mixed at 71:25:2:2 mole ratio. Total amount was 3 µmoles. Nitrogen flow was use to remove the liquid solvents, and lipids were then dried in vacuum for 2 h, followed by re-suspension with 500 µl buffer containing 50 mM HEPES, 140 mM KCl, and 10% glycerol. The resuspended lipids were treated with freezing (using liquid nitrogen) and thawing (in 37 °C water bath) cycles for 8 times, followed by extrusion using 100 nm or 50 nm membrane for 21 times.

Bilayer preparation and TIRF microscopy

Bilayers were prepared by bursting liposomes on the glass surface using a glass-bottomed µ-Slide $V1^{0.5}$ chip from Ibidi. 2.5 µl $MgCl_2$ at 500 mM were added into 122.5 µl buffer containing 50 mM HEPES (pH 7.4), 140 mM KCl, and 10% glycerol. Then 125 µl extruded bilayer liposomes were added. 60 µl $MgCl_2$-liposome solution were loaded into the channel of the ibidi chip and incubate for 40 min at room temperature. The channel was washed with the same buffer supplemented with 6 mM EDTA, and then with buffer supplemented with 1 mM TCEP.

The Ibidi chip was then mounted to the stage of a Nikon TIRF microscope. To monitor formation of clusters on the bilayer, a solution of 55 nM cytosolic Syt-1 in the buffer containing 50 mM HEPES 140 mM KCl, 10% glycerol, and 1 mM TCEP flowed into the channel of the Ibidi chip using a syringe drive at 30 ul/min. And the bilayer was imaged at room temperature with the TIRF microscope in real-time.

Counting Syt-1 copy numbers

There are two types of experiments in this paper: the equilibrium experiment where the sizes of the clusters remain constant, and the dynamic experiments where the clusters are in rapid growth or disassembly.

We have previously described the procedure for counting the copy number of molecules in clusters of various size for determining the sizes of clusters in equilibrium experiments[8]. Here is a brief description of the method.

Determination of the number of copies of Syt-1 in each cluster is achieved through counting the number of fluorophores in the cluster. We assume that the copy numbers of protein molecules and fluorophores are equal because all proteins in the experiments display very high labeling efficiencies (~95%).

For clusters at equilibrium, we gradually bleached the image frames using suitable laser power at different positions. The bleaching profiles of each particle (particle fluorescence intensity versus bleaching time) were plotted and two types of bleaching patterns were found, depending of the cluster size. When the protein copy number was small, the bleaching profile displayed apparent discrete steps (Fig. 1C). Then, the actual number of proteins can be determined from counting the number and intensity of steps. This approach only works for relatively small copy numbers (7 or fewer). When the copy number is large, the bleaching profile becomes smooth and can be fitted with an exponential decay function. The size of larger clusters can be calculated from the initial fluorescence intensity of the cluster at the beginning of bleaching, I_0. The copy number N is obtained through

$$N = I_0/a$$

where a is the unit intensity of a single fluorophore, i.e., the average intensity of a single bleaching step determined using small clusters[16].

Both method, step-bleaching and the method based on total intensity, provide similar results in the overlapping range 5–7 copies (see for instance Fig. 1C).

In this study we also counted copy numbers out of equilibrium in dynamic experiments (clusters that are in rapid formation and disassembly).

In these dynamic experiments, where we monitor the rapid association or dissociation process of clusters in real-time, we closed the shutter right after each data acquisition and ensured the laser power was sufficiently low to minimize photobleaching. Since it is not possible to use step-bleaching to determine the copy numbers of the clusters, the intensities of clusters

measured during their growth or disassembly provide a direct measure of their size at any time using the same equation:

$$N(t) = I(t)/a$$

In some cases, when the cluster size is small, it is possible to observe step-like dissociation (first two panels in Fig. 2C) or association (first two panels in Fig. 3C) because the Syt-1 molecules were usually separated from (dissociation) or added into (association) the cluster following the one-by-one pattern. Consequently, the copy number can also be counted from the number of steps.

GUV preparation

Giant unilamellar vesicles (GUVs) were used for HS-AFM. GUVs were prepared by electroformation using DOPC and DOPS mixtures[43]. 20 µl of 1 mg/ml lipid mix (DOPC:DOPS, 6:4, mol:mol) were deposited on two indium tin oxide (ITO)-coated glass slides (70–100 Ω resistivity, Sigma-Aldrich) and placed in a vacuum desiccator for at least 2 h to remove traces of organic solvent. An opened tor rubber joint of ~1 mm thickness was used as a non-leaky spacer between the two ITO slides, and the chamber was formed by compressing the two slides with spring metal clips. The chamber was filled with 400 µl of 300 mM sucrose solution and exposed to 1 V AC-current (10 Hz sinusoidal) at room temperature for 1.5 h. The resulting suspension was collected in a tube and used within the next days for experiments.

High-Speed Atomic Force Microscopy (HS-AFM) and data analysis

A mica disc of 1 mm diameter was glued to a 1 mm^2 x 3 mm^2 glass cylinder and used as sample stage. 1 µl of imaging buffer (25 mM HEPES pH 7.4, 1 mM DTT, 2 mM $Mg(C_2H_3O_2)_2$, 1 mM EDTA) was added to the freshly cleaved mica, followed by addition of 1 µl of the GUVs suspension prepared as described above. The sample was incubated for 10 min and gently rinsed with imaging buffer and always kept under fluid. The HS-AFM fluid chamber was then filled with ~120 µl imaging buffer into which the sample stage was immersed. First, the quality of SLB formation was checked by HS-AFM imaging. After SLB assessment and image acquisition area positioning, cytosolic Syt-1 was added to the fluid chamber to a final concentration of 500 nM. After imaging the Syt-1 clusters at Ca^{2+}-free condition, $CaCl_2$ was then added to the AFM fluid chamber to reach a final concentration of 2 mM. Prior to each experiment, the protein was dialyzed against imaging buffer for 1 h.

Imaging was performed at room temperature on an HS-AFM 1.0 (RIBM, Japan) using ~8 µm long cantilevers (NanoWorld, Switzerland) with a nominal resonance frequency of ~1.2 MHz and ~0.7 MHz in air and liquid, respectively, and a nominal spring constant of ~0.15 N/m[44]. To achieve minimum tip-sample interaction, small oscillation free (Afree) and set point (Aset) amplitudes of ~1 nm and ~0.9 nm, respectively, were used. Typically, pixel sampling ranged between 300 × 300 pixel and 200 × 200 pixel and frame acquisition rate ranged between 1 s^{-1} and 2 s^{-1}.

For HS-AFM movie analysis, we performed a moving average of 3 consecutive time frames to improve the signal-to-noise ratio and a first order polynomial flattening. Syt-1 size and diameter were manually measured using ImageJ. Calculation and representation of size and section profiles were performed in OriginLab (version 2019b).

Reporting summary

Further information on research design is available in the Nature Portfolio Reporting Summary linked to this article.

Data availability

Data reported in this study are available in the article and the supplementary information. The source data file underlying all graphs can be found in Supplementary Data. All other data are available from the corresponding author on reasonable request.

Received: 2 April 2024; Accepted: 25 November 2024;
Published online: 03 December 2024

References

1. Sakamoto, H. et al. Synaptic weight set by Munc13-1 supramolecular assemblies. *Nat. Neurosci.* **21**, 41–49 (2018).
2. Ryan, T. A. Munc13 marks the spot. *Nat. Neurosci.* **21**, 5–6 (2018).
3. Wang, J. et al. Calcium sensitive ring-like oligomers formed by synaptotagmin. *Proc. Natl Acad. Sci. USA* **111**, 13966–13971 (2014).
4. Willig, K. I., Rizzoli, S. O., Westphal, V., Jahn, R. & Hell, S. W. STED microscopy reveals that synaptotagmin remains clustered after synaptic vesicle exocytosis. *Nature* **440**, 935–939 (2006).
5. Desai, R. C. et al. The C2B domain of synaptotagmin is a Ca(2+)-sensing module essential for exocytosis. *J. Cell Biol.* **150**, 1125–1136 (2000).
6. Littleton, J. T. et al. synaptotagmin mutants reveal essential functions for the C2B domain in Ca2+-triggered fusion and recycling of synaptic vesicles in vivo. *J. Neurosci.* **21**, 1421–1433 (2001).
7. Zanetti, M. N. et al. Ring-like oligomers of Synaptotagmins and related C2 domain proteins. *Elife* **5**, e17262 (2016).
8. Li, F. et al. Vesicle capture by membrane-bound Munc13-1 requires self-assembly into discrete clusters. *FEBS Lett.* **595**, 2185–2196 (2021).
9. Grushin, K., Kalyana Sundaram, R.V., Sindelar, C.V. & Rothman, J.E. Munc13 structural transitions and oligomers that may choreograph successive stages in vesicle priming for neurotransmitter release. *Proc Natl Acad. Sci. USA* **119**, e2121259119 (2022).
10. Wang, S. et al. Munc18 and Munc13 serve as a functional template to orchestrate neuronal SNARE complex assembly. *Nat. Commun.* **10**, 69 (2019).
11. Ma, C., Su, L., Seven, A. B., Xu, Y. & Rizo, J. Reconstitution of the vital functions of Munc18 and Munc13 in neurotransmitter release. *Science* **339**, 421–425 (2013).
12. Liu, X. et al. Functional synergy between the Munc13 C-terminal C1 and C2 domains. *Elife* **5**, e13696 (2016).
13. Wang, S. et al. Conformational change of syntaxin linker region induced by Munc13s initiates SNARE complex formation in synaptic exocytosis. *EMBO J.* **36**, 816–829 (2017).
14. Ma, C., Li, W., Xu, Y. & Rizo, J. Munc13 mediates the transition from the closed syntaxin-Munc18 complex to the SNARE complex. *Nat. Struct. Mol. Biol.* **18**, 542–549 (2011).
15. Bera, M. et al. Two successive oligomeric Munc13 assemblies scaffold vesicle docking and SNARE assembly to support neurotransmitter release. *bioRxiv* https://doi.org/10.1101/2023.07.14.549017 (2023).
16. Li, F., Grushin, K., Coleman, J., Pincet, F. & Rothman, J. E. Diacylglycerol-dependent hexamers of the SNARE-assembling chaperone Munc13-1 cooperatively bind vesicles. *Proc. Natl Acad. Sci. USA* **120**, e2306086120 (2023).
17. Sudhof, T. C. & Rothman, J. E. Membrane fusion: grappling with SNARE and SM proteins. *Science* **323**, 474–477 (2009).
18. Zhou, Q. et al. Architecture of the synaptotagmin-SNARE machinery for neuronal exocytosis. *Nature* **525**, 62–67 (2015).
19. Zhou, Q. et al. The primed SNARE-complexin-synaptotagmin complex for neuronal exocytosis. *Nature* **548**, 420–425 (2017).
20. Yoshihara, M. & Littleton, J. T. Synaptotagmin I functions as a calcium sensor to synchronize neurotransmitter release. *Neuron* **36**, 897–908 (2002).
21. Fernandez-Chacon, R. et al. Synaptotagmin I functions as a calcium regulator of release probability. *Nature* **410**, 41–49 (2001).
22. Shao, X., Davletov, B. A., Sutton, R. B., Sudhof, T. C. & Rizo, J. Bipartite Ca2+-binding motif in C2 domains of synaptotagmin and protein kinase C. *Science* **273**, 248–251 (1996).
23. Brose, N., Petrenko, A. G., Sudhof, T. C. & Jahn, R. Synaptotagmin: a calcium sensor on the synaptic vesicle surface. *Science* **256**, 1021–1025 (1992).

24. Stein, A., Radhakrishnan, A., Riedel, D., Fasshauer, D. & Jahn, R. Synaptotagmin activates membrane fusion through a Ca2+-dependent trans interaction with phospholipids. *Nat. Struct. Mol. Biol.* **14**, 904–911 (2007).
25. Ramakrishnan, S. et al. Synaptotagmin oligomers are necessary and can be sufficient to form a Ca(2+) -sensitive fusion clamp. *FEBS Lett.* **593**, 154–162 (2019).
26. Ramakrishnan, S., Bera, M., Coleman, J., Rothman, J.E. & Krishnakumar, S.S. Synergistic roles of Synaptotagmin-1 and complexin in calcium-regulated neuronal exocytosis. *Elife* **9**, e54506 (2020).
27. Courtney, N. A., Bao, H., Briguglio, J. S. & Chapman, E. R. Synaptotagmin 1 clamps synaptic vesicle fusion in mammalian neurons independent of complexin. *Nat. Commun.* **10**, 4076 (2019).
28. Wang, J. et al. Circular oligomerization is an intrinsic property of synaptotagmin. *Elife* **6**, e27441 (2017).
29. Bello, O. D. et al. Synaptotagmin oligomerization is essential for calcium control of regulated exocytosis. *Proc. Natl Acad. Sci. USA* **115**, E7624–E7631 (2018).
30. Tagliatti, E. et al. Synaptotagmin 1 oligomers clamp and regulate different modes of neurotransmitter release. *Proc. Natl Acad. Sci. USA* **117**, 3819–3827 (2020).
31. Li, X. et al. Symmetrical organization of proteins under docked synaptic vesicles. *FEBS Lett.* **593**, 144–153 (2019).
32. Courtney, K.C. et al. Synaptotagmin 1 oligomerization via the juxtamembrane linker regulates spontaneous and evoked neurotransmitter release. *Proc Natl Acad. Sci. USA* **118**, e2113859118 (2021).
33. Li, F., Tiwari, N., Rothman, J. E. & Pincet, F. Kinetic barriers to SNAREpin assembly in the regulation of membrane docking/priming and fusion. *Proc. Natl Acad. Sci. USA* **113**, 10536–10541 (2016).
34. Takamori, S. et al. Molecular anatomy of a trafficking organelle. *Cell* **127**, 831–846 (2006).
35. Wilhelm, B. G. et al. Composition of isolated synaptic boutons reveals the amounts of vesicle trafficking proteins. *Science* **344**, 1023–1028 (2014).
36. Rothman, J. E., Krishnakumar, S. S., Grushin, K. & Pincet, F. Hypothesis - buttressed rings assemble, clamp, and release SNAREpins for synaptic transmission. *FEBS Lett.* **591**, 3459–3480 (2017).
37. Rothman, J.E., Grushin, K., Bera, M. & Pincet, F. Turbocharging synaptic transmission. *FEBS Lett* **597**, 2233–2249 (2023).
38. Li, F. et al. A Half-Zippered SNARE Complex Represents a Functional Intermediate in Membrane Fusion. *J. Am. Chem. Soc.* **136**, 3456–3464 (2014).
39. Crowley, J. J., Carter, A. G. & Regehr, W. G. Fast vesicle replenishment and rapid recovery from desensitization at a single synaptic release site. *J. Neurosci.* **27**, 5448–5460 (2007).
40. Gruget, C. et al. Rearrangements under confinement lead to increased binding energy of Synaptotagmin-1 with anionic membranes in Mg(2+) and Ca(2). *FEBS Lett.* **592**, 1497–1506 (2018).
41. Gruget, C. et al. Synaptotagmin-1 membrane binding is driven by the C2B domain and assisted cooperatively by the C2A domain. *Sci. Rep.* **10**, 18011 (2020).
42. Ji, H. et al. Protein determinants of SNARE-mediated lipid mixing. *Biophys. J.* **99**, 553–560 (2010).
43. Mathivet, L., Cribier, S. & Devaux, P. F. Shape change and physical properties of giant phospholipid vesicles prepared in the presence of an AC electric field. *Biophys. J.* **70**, 1112–1121 (1996).
44. Colom, A., Redondo-Morata, L., Chiaruttini, N., Roux, A. & Scheuring, S. Dynamic remodeling of the dynamin helix during membrane constriction. *Proc. Natl Acad. Sci. USA* **114**, 5449–5454 (2017).

Acknowledgements

This work was supported by National Institute of Health (NIH) grant DK027044.

Author contributions

F.L., F.P., and J.E.R. designed the study; F.L., J.C., L.R.M., R.V.K.S., and E.S. performed experiments; F.L., L.R.M., F.P., and J.E.R. analyzed data; and F.L., F.P., and J.E.R. wrote the manuscript.

Competing interests

The authors declare no competing interests.

Additional information

Supplementary information The online version contains supplementary material available at https://doi.org/10.1038/s42003-024-07317-9.

Correspondence and requests for materials should be addressed to James E. Rothman or Frédéric Pincet.

Peer review information *Communications Biology* thanks Cong Ma and the other, anonymous, reviewer(s) for their contribution to the peer review of this work. Primary Handling Editors: Huan Bao and Ophelia Bu.